A Sparse Sampling Sensor Front-end IC for Low Power Continuous SpO$_2$ & HR Monitoring

Sina Faraji Alamouti, *Student Member, IEEE*, Jasmine Jan, *Student Member, IEEE*, Cem Yalcin, *Student Member, IEEE*, Jonathan Ting, Ana Claudia Arias, *Senior Member, IEEE*, Rikky Muller, *Senior Member, IEEE*

Abstract—Photoplethysmography (PPG) is an attractive method to acquire vital signs such as heart rate and blood oxygenation and is frequently used in clinical and at-home settings. Continuous operation of health monitoring devices demands a low power sensor that does not restrict the device battery life. Silicon photodiodes (PD) and LEDs are commonly used as interface devices in PPG sensors; however, using of flexible organic devices can enhance the sensor conformality and reduce the cost of fabrication. In most PPG sensors, most of system power consumption is concentrated in powering LEDs, traditionally consuming mWs. Using organic devices further increases this power demand since these devices exhibit larger parasitic capacitances and typically need higher drive voltages. This work presents a sensor IC for continuous SpO$_2$ and HR monitoring that features an on-chip reconstruction-free sparse sampling algorithm to reduce the overall system power consumption by ∼70% while maintaining the accuracy of the output information. The designed frontend is compatible with a wide range of devices from silicon PDs to organic PDs with parasitic capacitances up to 10 nF. Implemented in a 40 nm HV CMOS process, the chip occupies 2.43 mm^2 and consumes 49.7 W and 15.2 W of power in continuous and sparse sampling modes respectively. The performance of the sensor IC has been verified *in vivo* with both types of devices and the results are compared against a clinical grade reference. Less than 1 bpm and 1% mean absolute errors were achieved in both continuous and sparse modes of operation.

Index Terms—PPG, SpO$_2$, Heart Rate, Sensor IC, Sparse Sampling, Organic Devices, Low Power

I. INTRODUCTION

TIMELY diagnosis of many chronic cardiovascular and respiratory systems diseases can be enabled through continuous monitoring of vital signs such as heart rate (HR), blood oxygenation level (SpO$_2$), respiration rate, blood pressure etc. [1]–[6]. A comfortable, wearable device can track these vital signs autonomously, unobtrusively, and without the users intervention, allowing changes to be immediately detected and reported to medical staff, preventing disease progression. Similarly in patients with a history of heart failure, remote monitoring of vital signals has proven essential in early recognition of potential congestions [2], [6]. Moreover, in the setting of COVID-19, remote monitoring provides the healthcare workforce with real-time biodata without needing any physical contact, reducing the spread of infection [3]. As a result, the interest and market for biosensors in at home care continue to grow. A similar trend is observed for

S.F. Alamouti, J. Jan, C. Yalcin, J. Ting, A.C.Arias, and R. Muller are with the Department of Electrical Engineering and Computer Sciences, University of California, Berkeley, Berkeley, CA USA 94720

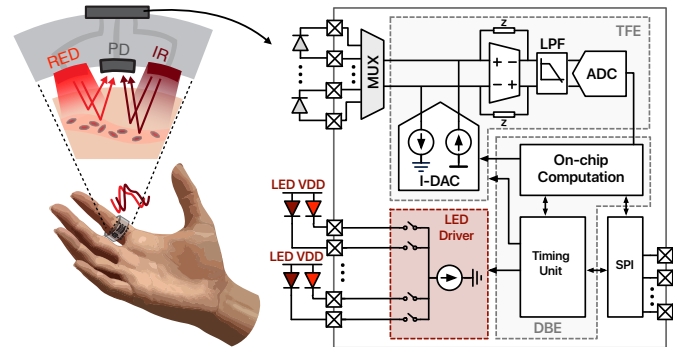R. Muller is with Chan-Zuckerberg Biohub, San Francisco, CA USA 94158.

Fig. 1. Reflectance mode pulse oximetry and typical SpO$_2$ sensing IC block diagram.

health monitoring wearable devices including smart-watches, rings, and health patches [4]. These devices aim to record a users vital signs without their intervention. The biodata is recorded, stored, and presented to the user via application interfaces and can be used to warn users of an abnormal condition. Traditionally, electrocardiography (ECG) has been used to accurately measure HR and cardiac waveforms; since it requires access to multiple sites across the body, the subject has to trigger these measurements and thus, it cannot be performed continuously. Photoplethysmography (PPG) is an attractive method to acquire biodata such as HR due to its fully optical, non-invasive nature where the sensors do not even need to contact the subject skin. In addition, using light from two distinct wavelengths, typically red and infra-red (IR), the SpO$_2$ of the subject can be extracted, a technique known as pulse oximetry. Figure 1 shows the operation of a pulse oximeter where light sources, typically LEDs, are driven sequentially and the reflected light is received by a photodiode (PD), inducing a photocurrent that contains the PPG signal. A current sensing IC, shown in figure 1, then samples and digitizes the photocurrent to output the information.

Silicon PDs and LEDs are commonly used in todays SpO$_2$ sensors. Despite great responsivity and mm-scale sizes, they are rigid devices that eventually impact the dimensions and conformality of the sensor. Organic optical devices however are lightweight, mechanically flexible, and shock resistant, and thus offer a more conformal solution, improving user comfort [7]–[9]. Flexible vital sign monitoring patches can therefore be built to seamlessly integrate into clothing and be comfortably worn over long durations [9], [11]. In addition, these devices can be printed using low-cost fabrication processes, reducing the overall cost of the health monitoring patches [12]–[14].

Commercial SpO$_2$ sensors operate with mWs of power to drive the LEDs posing strict limits on the sensor battery life. Use of OLEDs further restricts the battery life as these devices generally require higher drive voltages, up to 8 V [9], [10]. Duty cycling has been used in prior arts [15], [16] to lower the power consumption of the overall system at the cost of increased noise bandwidth, impacting signal-to-noise ratio (SNR). The parasitic capacitance of the PD (C$_{\mathrm{Par}}$) impacts the input referred noise of the transimpedance amplifier (TIA) by attenuating the feedback factor as the frequency increases [17]. C$_{\mathrm{Par}}$ in silicon PDs ranges from sub-pF to 100s of pF depending on the size of their active area. OPDs however exhibit a much larger C$_{\mathrm{Par}}$ up to 10 nF which can exceed the maximum capacitance handled by many of the prior arts. It is thus critical that a sensor IC aimed for a wearable can operate with a wide variety of devices and a wide range C$_{\mathrm{Par}}$.

On-chip photodetectors were employed to significantly lower the detector and the interface parasitic capacitance and as a result compensate the SNR penalties at extremely low duty cycle ratios [15], [18]. However, on-chip photodiodes generally offer inferior responsivities compared to their off-the-shelf counterparts, reducing the power saving benefits of this approach. In addition, there are fundamental limitations on how fast the LEDs can operate as well as the response bandwidth of the PDs, restricting the lower bound of the duty cycle. Moreover, this technique cannot be extended to using organic devices as they are usually fabricated on plastic substrates. [19] tried to balance the tradeoff between SNR and the LEDs and readout power by setting the front-end bias current. The technique significantly reduced the readout power, but the LEDs still dominated the sensor power consumption. Compressive sampling was first introduced in [20] to exploit the sparse nature of the PPG signal and thus save power by reducing the number of sample points. Despite excellent results for HR estimation from the compressively sampled data, SpO$_2$ measurements required full reconstruction of the PPG waveform out of randomly selected samples, demanding up to 10 mW of processing power [20]. [21] presented the heart-beat-locked-loop technique to make the sensor lock to the PPG signal period and selectively sample the PPG peaks to report HR data. A comparator-based design was used that only detected the input peaks, outputting a digital clock that was synchronized to the input period. This lowered the LED power by a factor of ~6.5×, but since the PPG waveform was not digitized, no SpO$_2$ measurements were performed.

This work presents an SpO$_2$ and HR monitoring IC utilizing a reconstruction-free sparse sampling algorithm to reduce the overall system power consumption by about 70% [22]. This manuscript is organized as follows. Section II outlines the system requirements and the overall architecture of the sensor. In section III, the proposed sparse sampling algorithm is discussed. Section IV describes the circuit-level details of the implemented IC. Bench-top electrical and *in vivo* measurement results are presented in section V followed by the conclusions and comparison against selected prior arts in section VI.

II. SYSTEM OVERVIEW

A. System requirements

As discussed in [23], the PD photocurrent contains multiple components including the detector dark current, the ambient photocurrent, and the reflected lights baseline (I$_{\mathrm{DC}}$) and pulsatile (I$_{\mathrm{AC}}$) components. The overall input baseline component is commonly 40-60 dB stronger than the pulsatile signal. Thus, without any subtraction, the readout chain will need a very large dynamic range, greater than 100 dB [24], which can pose challenges in realizing a low power readout.

The PPG I$_{\mathrm{AC}}$ is a low frequency signal with most of its power residing between 0.5 to 5 Hz, which according to the Nyquist theorem can be sampled with frequencies as low as 10 Hz. However, as explained in [21], the timing resolution of the PPG samples can impact the accurate detection of pulsatile peaks, which in turn affects the reported HR error of the sensor. Therefore, a sampling frequency of a few 10s to 100s of Hz is typically selected. In this work, to achieve an average HR error of less than 1 bpm, a sampling rate of 100 S/s is used. Furthermore, to extract SpO$_2$ with a 2% error, the sensor requires nearly 40 dB of SNR [25], which determines the noise level of the readout. The amplitude of I$_{\mathrm{AC}}$ depends on many biological factors such as the structure, thickness, and color of Epidermis and Dermis, optical factors such as wavelength of light and devices' responsivities, and mechanical factors such as distance between the sensor and tissue as well as the angle of emission. These factors cause the I$_{\mathrm{AC}}$ to vary over a wide range from a few nAs to up to 100s of nAs. Thus, to maintain the required SNR for low amplitude inputs, the readout input referred noise density needs to be approximately 1-10 pA/rtHz.

B. Sensor architecture

The block diagram of a typical SpO$_2$ sensing IC is shown in figure 1. LEDs are driven sequentially using on-chip current sources, emitting light at red (660 nm) or green (530nm) as well as IR (880 nm) wavelengths to the tissue. The received photocurrent with a baseline component as large as a few μAs is digitized by the readout. To relax the dynamic range requirements of the chain, the large input DC component is subtracted using differential current DACs (I-DACs). The remaining AC component is then amplified, filtered, and digitized through the readout chain. On-chip digital back-end computes the required code for the DACs, closing the servo-loop. The digitized data is transmitted to an FPGA or a PC via a serial programming interface.

Large values of C$_{\mathrm{Par}}$ are an obstacle in achieving low input referred noise in current sensing frontends. Furthermore, C$_{\mathrm{Par}}$ poses a constraint on the achievable transimpedance gain and bandwidth in the TIA. As a result, handling very large values of C$_{\mathrm{Par}}$ as in OPDs necessitates careful design of the TIA and readout chain. Prior arts have used both capacitive and resistive feedback types in the TIA architecture. Traditionally, TIAs with capacitive feedback (CTIA) are deployed to achieve the lowest input referred current noise [17]. However, most CTIA designs only handle a few pFs of parasitic capacitance at the TIA input. In order to acquire the current signal out of OPDs with up to 10 nF of C$_{\mathrm{Par}}$, such topologies would require
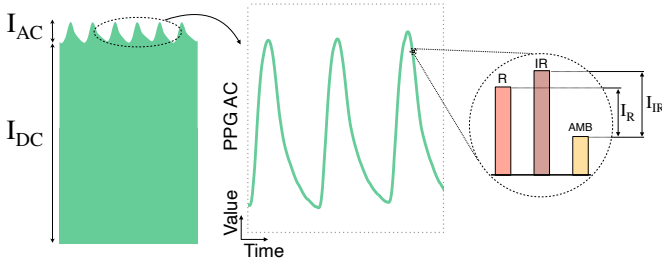
Fig. 2. PPG signal AC and DC components. Red and IR signals are computed after subtracting the AMB sample, performing system level CDS.
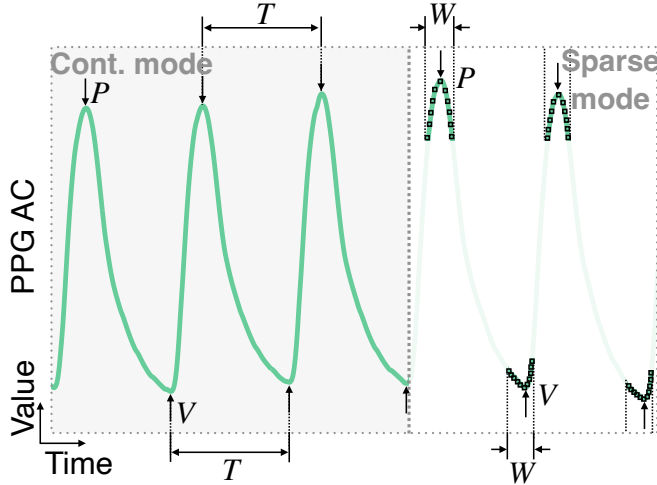

Fig. 3. Sparse sampling algorithm. The sensor transitions to sparse mode after learning T over multiple cycles where it predicts next PAVs.

very large values of feedback and load capacitors (100s of pF) to deliver the required noise performance while realizing a reasonable gain. This can result in very large area occupation and demand larger transconductances, increasing the overall power consumption of the TIA. In resistive-capacitive TIAs (ZTIA), the feedback resistor enhances the feedback factor at lower frequencies. This causes the output noise spectrum to only increase at high frequencies, a phenomenon known as noise peaking. The output noise PSD of the ZTIA can be written in a simplified form as follows:

$$S_{N_{out}}(f) \approx 4kT \left(\frac{1}{g_m} + R_F \right)$$

$$\times \left(\frac{4\pi^2 \frac{R_F}{g_m} C_{Par}^2 f^2 + 1}{16\pi^4 C_F^2 C_{Par}^2 \frac{R_F^2}{g_m^2} f^4 + 4\pi^2 \left(\frac{C_{Par}^2}{g_m^2} + R_F^2 C_F^2 \right) f^2 + 1} \right)$$

$$(1)$$

with g_m, R_F, and C_F representing the effective transconductance of the OTA, the feedback resistance and capacitance. Only the OTA thermal noise as well as the feedback resistors Johnson noise is considered in this analysis. The bandwidth of this noise peaking can be greater than the systems observation bandwidth. It is therefore possible to attenuate the TIAs high frequency noise by means of sufficient filtering through the subsequent blocks. The appendix section covers the derivation of (1) as well as the comparison between CTIA and ZTIA topologies in greater detail. As a result, a ZTIA readout chain can potentially deliver a lower input referred noise compared to CTIA based architectures when C_{Par} is very large and is

hence chosen in this design.

Like OPDs, OLEDs tend to have very large parasitic capacitances that take time to charge up, increasing the system settling time. Therefore, these parasitic elements slow down the sensor and limit the minimum duty cycle ratio of the system, thereby demanding more power. In addition, OLEDs typically require higher drive voltages up to 8 V [9], [10] that further increase the sensor power consumption. It is therefore crucial to come up with strategies to alleviate the power requirements. The following section discusses a specific sparse sampling algorithm, implemented in this work, that aims to reduce the number of samples in the system and consequently save power.

III. SPARSE SAMPLING OF PPG SIGNAL

A. HR and SpO2 extraction

Figure 2 shows a typical PPG waveform containing both AC and DC components. The period (T) of the AC component represents a heart-beat cycle and can be used to compute HR. Thus, PPG using a single LED is sufficient to provide HR information. Prior arts have routinely used the average value of the period over 2 or 8 second windows. In this paper, an 8 second window is selected to report HR. (Eq. 2)

$$HR = \frac{60}{\overline{T}} \qquad (2)$$

SpO2, however, depends on relative concentration of oxygenated versus de-oxygenated hemoglobin, and hence, needs information at two different light wavelengths. As light passes through the tissue, it is attenuated by different elements and this attenuation is described by the extinction coefficient. Light at red and IR wavelengths have been used traditionally [26] since they offer the largest difference in extinction coefficients when passing through oxygenated and de-oxygenated hemoglobin. The value of SpO2 is computed based on the ratio of AC component over the DC component of red and IR PPG waveforms (Eq. 3-4). [9]

$$R_{OS} = \frac{I_{AC_{Red}}}{I_{DC_{Red}}} \bigg/ \frac{I_{AC_{IR}}}{I_{DC_{IR}}} \qquad (3)$$

$$SpO_2 = \frac{\varepsilon_{Hb_{Red}} - \varepsilon_{Hb_{IR}} \cdot R_{OS}}{\varepsilon_{Hb_{Red}} - \varepsilon_{HbO2_{Red}} + [\varepsilon_{Hb_{IR}} - \varepsilon_{HbO2_{IR}}] \cdot R_{OS}} \qquad (4)$$

where ε is the extinction coefficient of light at red or IR wavelength through oxygenated or de-oxygenated hemoglobin. To compute SpO2, only the peak and valley (PAV) values of the PPG signals are needed in the two wavelengths. It is therefore possible to only sample the signal PAVs and as a result save power.

B. Sparse sampling algorithm

The idea of the proposed sparse sampling algorithm is shown in figure 3 where the sensor has two modes of operation. The flowchart of this sparse sampling algorithm is also shown in figure 4. The sensor starts by uniformly sampling the PPG signal at 100 Hz (continuous mode). The period of the AC component (T) is learned over multiple cycles.
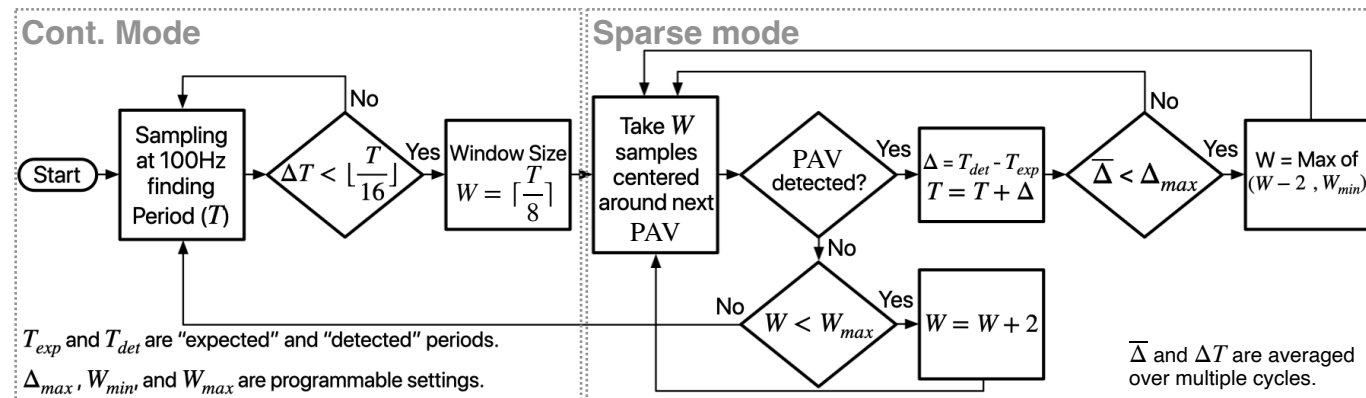
Fig. 4. Sparse sampling algorithm flow-chart.

Once a stable value is realized, the sensor enters the sparse mode where it predicts the upcoming PAVs and takes a few samples centered around them. A window size (W) of $\lceil T/8 \rceil$ is initially selected which can then be reduced upon successful detection of PAVs. A smaller W means that fewer samples are taken and as a result the overall power is decreased. However, larger W allows the backend to accurately detect PAVs in the presence of high heart rate variability. Therefore, cycle-to-cycle updates are made to the estimated value of T to adjust for any period drift. If PAVs are repeatedly missed due to rapid drifts or large motion artifacts, the sensor expands its observation window by increasing W until a programmable maximum, W_{Max}. Without new PAVs detected, the sensor can revert to the continuous mode to re-learn T. The computed T, together with samples taken from signals PAVs are adequate to provide both HR and SpO$_2$ information.

Proper detection of PAVs by the backend depends on the SNR of the sparse samples as well as how fast the input is changing. To evaluate the performance of the proposed algorithm at different SNR levels and a range of HR values, a set of MATLAB simulations are run that quantify the reported HR error. The results of such simulations provide information about the required SNR levels at different heart rates to achieve the desired 1 bpm accuracy. These simulations were run with a sine wave input at frequencies ranging from 0.5 to 3 Hz, corresponding to HRs of 30 to 180 bpm, and at

amplitudes corresponding to SNRs from 28 to 56 dB. In each run, sparse sampling is performed on the sine wave input and the estimated periods are recorded, averaged over 8 second windows. A total of 12,800 simulations were conducted to capture the mean and variance of the reported HR errors. The results are shown in figure 5, where the solid lines show the mean error, and the green shades represent the $\pm 3\sigma$ of the computed HR errors. The results confirm that the proposed algorithm provides a robust operation under a wide range of SNR and heart rates. Furthermore, the results demonstrate that a minimum SNR of $\sim$30 dB is sufficient in achieving sub-1 bpm HR error for HRs up to 180 bpm. A similar test is performed in measurements to quantify the performance of the sensor and the results will be discussed in section V.

IV. CIRCUIT IMPLEMENTATION

A. Frontend architecture

Figure 6(a) shows the detailed block diagram of the transimpedance frontend (TFE) as well as the on-chip digital back-end (DBE). The PD is connected and read out differentially at the input. This eliminates the need for a separate low noise bias voltage on the other end of the detector. The 0 V bias also minimizes the PD dark current. 8-bit (5-bit thermometer/3-bit binary coded) differential I-DACs (P and N-DACs) subtract the DC component at the input up to 15 μA. The I-DAC LSB reference current is tunable from 20 to 60 nA to provide a wider range and granularity for the subtraction. N and P I-DAC codes are computed separately to adjust for any mismatch and gain error between them. This calibration only occurs once and the resulting coefficients are programmed into the backend. The DC DAC code for each phase is computed, stored, and updated separately for fastest operation. I-DAC codes are also re-timed prior to entering the DACs to enhance synchronicity and prevent race related glitches. The bandwidth of the servo-loop is set via a programmable digital attenuation in the feedback path to have a high-pass corner of $\sim$0.1 Hz. The remaining AC component of the signal is then amplified via a differential ZTIA followed by a reset integrator that provides additional gain and boxcar averaging, obviating the need for an explicit anti-alias filter. A 12-bit synchronous SAR ADC samples the integrator output and delivers the digital code to the DBE.
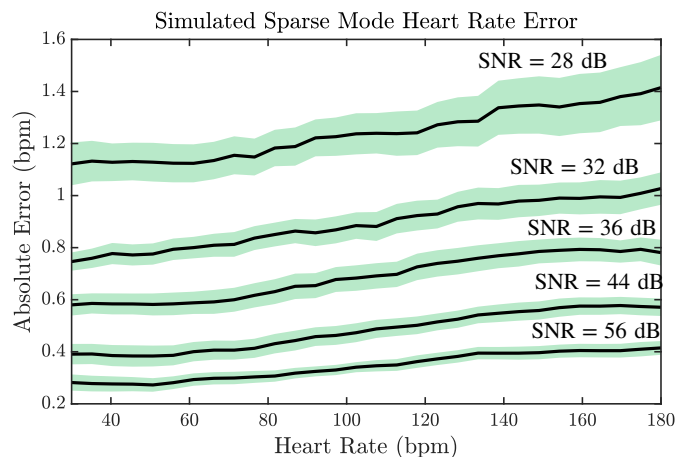

Fig. 5. Simulated sparse mode HR error for input sine waves at different frequencies and SNRs. Green shades show the $\pm 3\sigma$ range of the error.
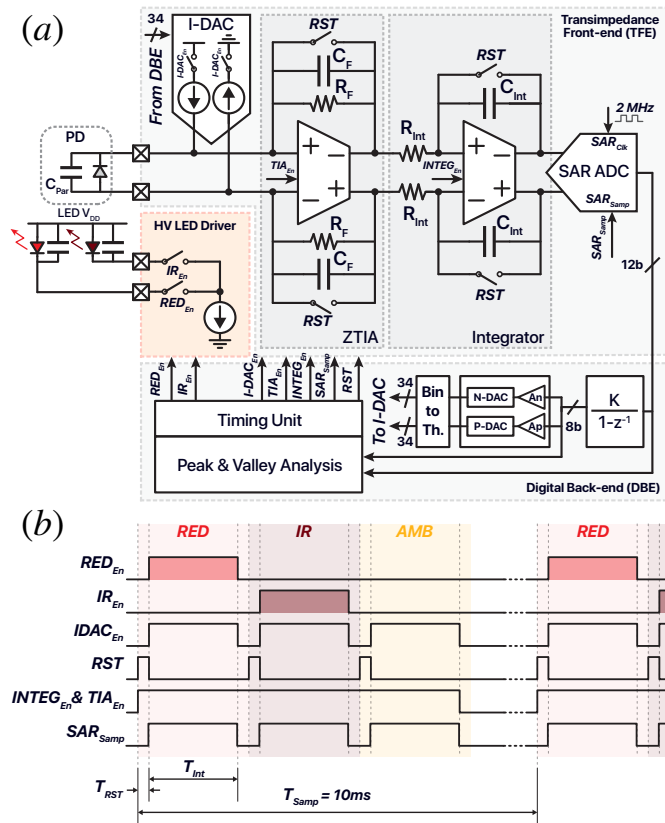
Fig. 6. Detailed channel block diagram (a) and timing diagram (b).

The timing of TFE operation is diagrammed in figure 6(b). Every sample consists of three back-to-back phases. Red and IR signals are acquired followed by an ambient (AMB) phase where no LED is on and the photocurrent due to the ambient light as well as the PD dark current are sampled. AMB must be sampled with each red/IR sample since there can exist time-varying changes in the ambient lighting as well as reflected pulsatile components during this phase. AMB subtraction also serves as a system level correlated double sampling (CDS) that helps remove any offset and flicker noise [16]. T_{RST} and T_{Int} are programmable settings that set the reset and integration durations for TFE. In most measurements, T_{Int} is set from 25 μs to 100 μs with T_{RST} as short as 5 to 10 μs. An on-chip timing unit provides all timing signals to the TFE and LED driver sub-blocks to maintain synchronicity. A peak and valley analysis block within the DBE performs algorithm computations and triggers counters that determine the upcoming sampling windows.

B. ZTIA design

As previously discussed, a ZTIA topology is utilized to accommodate a wide range of photodiode capacitance (C_{Par}) while maintaining a high SNR. The use of a resistor in the feedback eliminates the reset noise (kT/C) and the need for a separate CDS phase. Figure 7(a) shows the schematic of the 3-stage current reuse core OTA. The current reuse topology enhances the performance by doubling the effective current efficiency factor (g_m/I_D) of each stage. The fully differential architecture also provides better immunity against supply and common mode noise sources, as well as improved linearity.
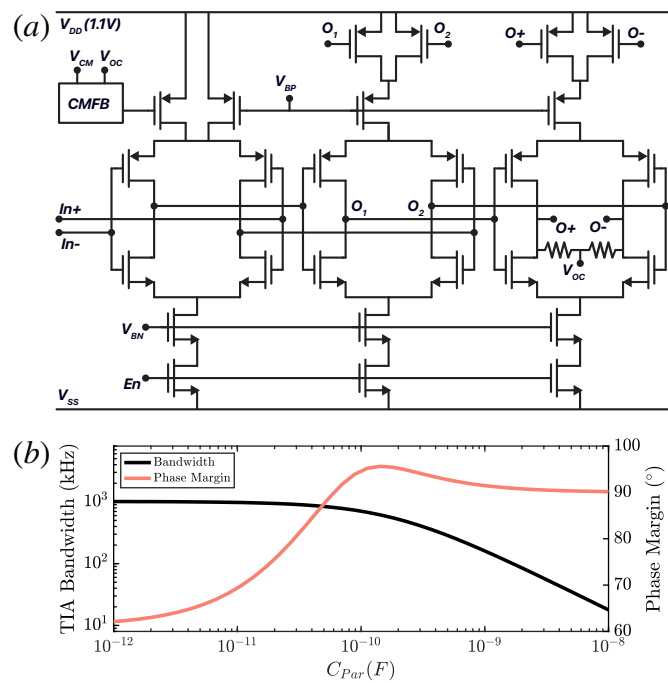

Fig. 7. (a) Schematic of the ZTIA core OTA. Current reuse topology enhances current efficiency and reduces power. (b) Post-extraction simulated TIA bandwidth and phase margin vs. C_{Par}

Figure 7(b) plots the closed-loop bandwidth and phase margin (PM) of the TIA for C_{Par} ranging from 1 pF to 10 nF. As shown, larger values of C_{Par} reduce the overall bandwidth and as a result increase the PM. The loop maintains a minimum PM of 62° across the entire C_{Par} range. Local and global common mode feedback networks are included to provide common mode bias and improve common mode rejection. Reset switches connect the inputs and outputs of the TIA during the RST phases to quickly bring the outputs to the mid-rail bias point. Values of R_F and C_F are tunable to provide a gain of 1 to 5 MΩ and an adjustable bandwidth. The entire OTA is power gated using low resistance NMOS transistors to save power outside of sampling windows.

C. Reset integrator and SAR ADC

The RC integrator captures the TIA output over T_{INT} and provides differential outputs to the SAR ADC sampling capacitors. A SAR topology is selected to achieve a low power consumption while providing the required resolution. The value of C_{Int} is tunable to allow for adjustable gain. The integrator is reset at the beginning of every phase via the RST switches. This integration and reset provides a boxcar averaging transfer function detailed in Eq. (5).

$$H_{Sinc}(f) = \frac{T_{Int}}{R_{Int} \cdot C_{Int}} \cdot Sinc(T_{Int} \cdot f) \qquad (5)$$

This low pass transfer function significantly attenuates the high frequency noise content of the TIA output. The feedback capacitors are sized such that the reset kT/C noise of the integrator is insignificant when referred to the channel input. Similar to the OTA, the integrator is shut down outside of sampling windows to save power. A 12-bit synchronous SAR ADC is implemented using monotonic switching scheme that
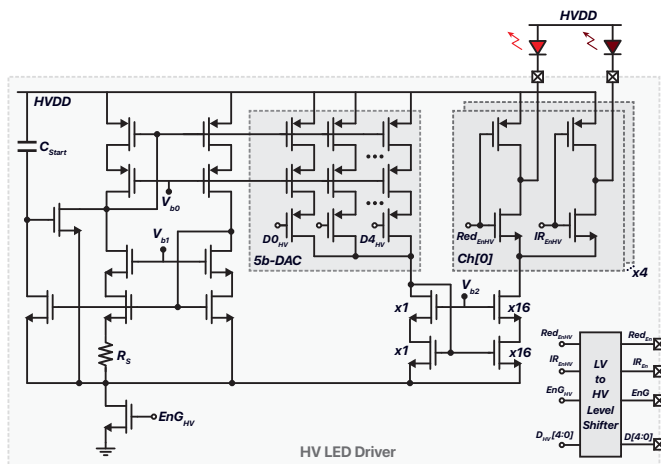
Fig. 8. The schematic of the HV LED driver is shown.

only needs half the total capacitance compared to traditional switching methods. The SAR ADC uses a 2 MHz reference clock provided by the DBE to perform the conversions.

D. Peripheral circuits

An on-chip PTAT current reference is used to supply the bias current of all analog sub-blocks. The PTAT nature of the reference increases the bias current in proportion to the temperature to maintain a constant noise level in the readout chain. An on-chip HV LED driver, shown in figure 8 is implemented to drive the LEDs with up to 16 mA of current. The driver uses HV transistors that operate with up to 8 V of supply voltage, enabling the use of OLEDs. The driver is controlled by the timing unit and sinks the current from the LEDs. The drive strength is 5-bit tunable and is separately set for red and IR phases.

V. MEASUREMENT RESULTS

A. Chip micrograph and power breakdown

The IC was fabricated in a TSMC 40 nm HV technology and occupies an area of 1.35×1.8 mm^2. Figure 9 shows the chip micrograph as well as the TFE and system power breakdown. In continuous mode, the sensor consumes a total of 49.7 μW with 45.1 μW, 1.22 μW, and 3.34 μW drawn by the two LEDs, the TFE, and the DBE respectively. Sparse mode lowers the system power consumption to 15.2 W with LEDs and TFE power going down by $\sim$75%, and the DBE power increasing by only 2%. The pie chart in figure 9 shows the breakdown of power consumption of the individual sub-blocks within the TFE in continuous mode where most of the power is dissipated in the ZTIA to maintain a low input referred noise.

B. Electrical measurements

The performance of the TFE was characterized via benchtop electrical measurements and the results are presented. Figure 10(a) shows the input referred noise (IRN) spectrum of the readout at 40 MΩ of overall gain. The measurement was performed with a C_{Par} = 40 pF matching the capacitance of the commercial PD. It achieved a noise spectrum density of

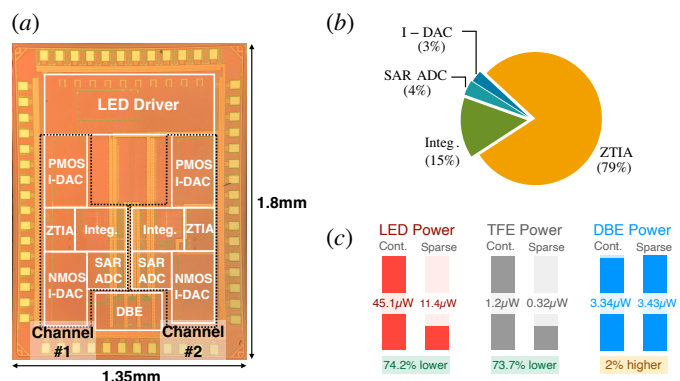Fig. 9. Chip micrograph (a). TFE power breakdown in continuous mode. (b) System power reduction between continuous mode and sparse mode. (c)

4.8 pA/rtHz and 10.8 pA$_{rms}$ integrated noise over the 5 Hz bandwidth. IRN increased with C_{Par} as plotted in figure 10(b) for C_{Par} as large as 10 nF, the largest measured capacitance of the OPDs [9], [10]. The ADC output spectrum for a 2 Hz sine wave input with 50 nA$_{pp}$ of amplitude is shown in figure 10(c). The TFE achieved an SFDR of 68.3 dB and an SNDR of 62.4 dB with the 3rd harmonic forming the largest spur.

The simulation results from section III (figure 5) were verified via similar benchtop measurements. A set of 48 measurements were performed while providing a sine wave to the TFE with sparse mode enabled. The frequency of the sine wave was swept from 0.5 to 3 Hz, corresponding to 30 to 180 bpm HR. Two different amplitudes were selected for the input sine wave to achieve two distinct SNR levels, 32 dB and 44 dB. Figure 11 presents the measured effective HR
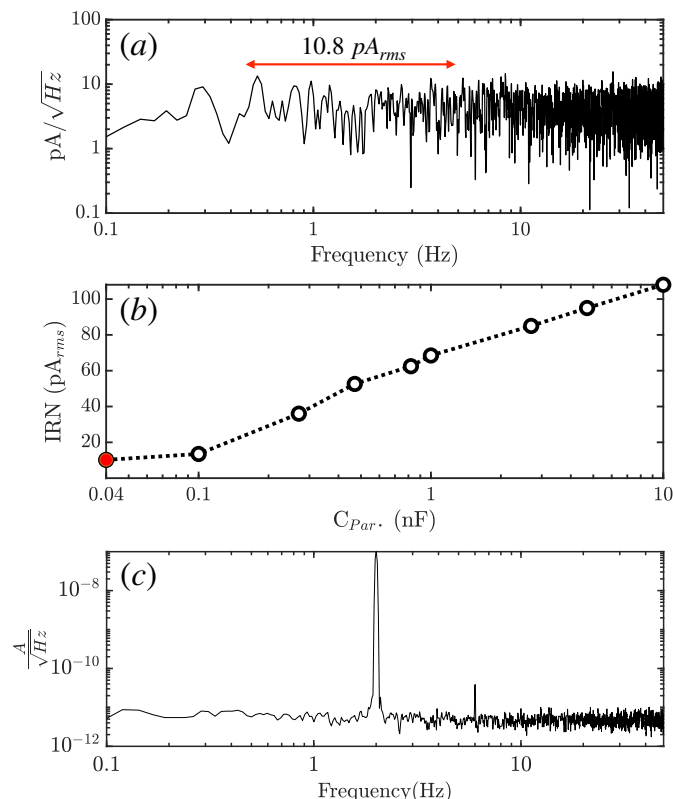

Fig. 10. Electrical testing results. (a) IRN spectrum for a 40 pF C_{Par}. (b) Integrated IRN over 5 Hz bandwidth vs. C_{Par}. The red dot corresponds to the spectrum from (a) (c) ADC output spectrum for a 2 Hz sine wave input.
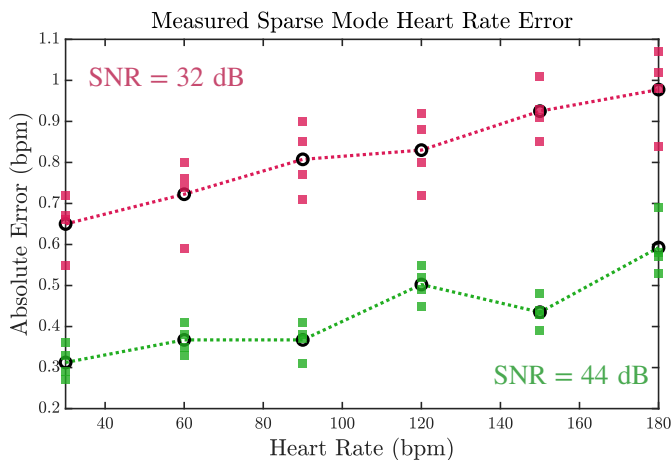
Fig. 11. Measured sparse mode HR error with input sine waves at different frequencies and at two levels of SNR. Black circles show the average error at each rate. The computed error is the mean absolute error over 8 s windows.

error for every experiment. The measured results are well in agreement with the simulation, confirming the performance and robustness of the algorithm. Less than 1 bpm of average error was measured with an SNR as low as 32 dB for HR up to 180 bpm.

C. In vivo results

A set of *in vivo* experiments were performed with the sensor in both continuous and sparse modes of operation. In these experiments, the sensor was placed on the index finger of a healthy adult in a sitting position, under typical incandescent
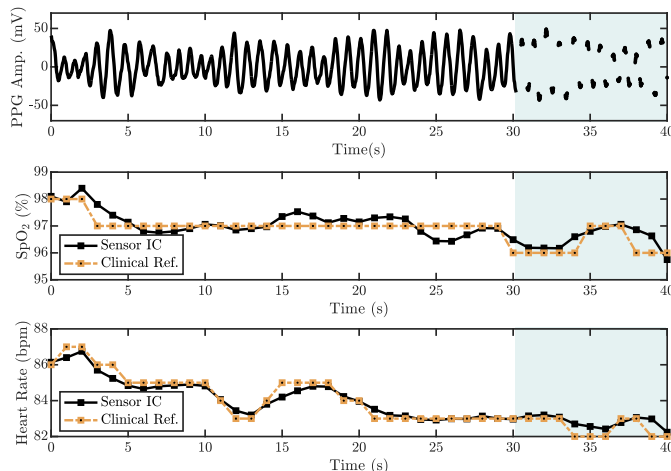

Fig. 12. *In vivo* verification of the sensor IC in both continuous and sparse modes using commercial silicon PD and LEDs. The PPG waveform and its corresponding HR and SpO$_2$ measurements are shown.
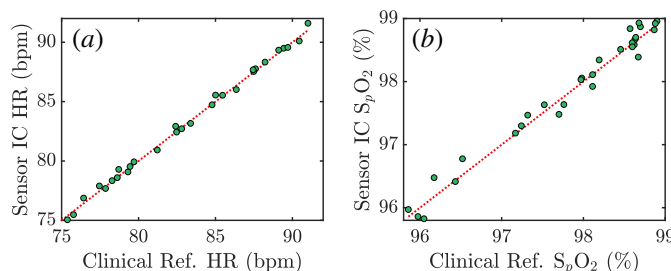

Fig. 13. HR and SpO$_2$ measurements from a set of 30 recordings using silicon PD and LEDs. The red dotted line shows the fit line.
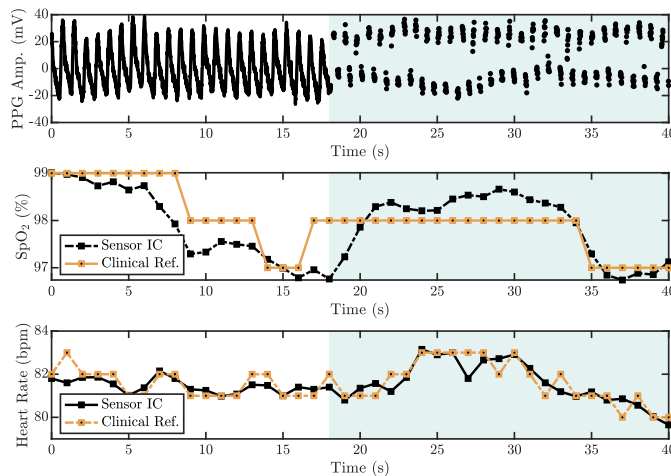

Fig. 14. *In vivo* verification of the sensor IC in both continuous and sparse modes using organic interface devices (OLEDs & OPDs). The PPG waveform and the corresponding HR and SpO$_2$ measurements are shown.

lighting and at room temperature. To evaluate the accuracy of the sensor output, a clinical grade pulse-oximeter (Wellue HPO) was attached to the subjects ring finger to perform measurements simultaneously with the sensor IC. In the first experiment, commercial PDs and LEDs were used as interface devices and the PPG signal, the HR, and the SpO$_2$ results were recorded. Figure 12 plots these results against data from the clinical reference. The accuracy of the sensor was maintained after transitioning to sparse mode where the HR and SpO$_2$ mean absolute errors only rose from 0.3 bpm and 0.5% to 0.4 bpm and 0.7% respectively. The errors were computed based on the total 40 seconds duration of the recording presented in figure 12 in both modes of operation. Figure 13 shows a set of
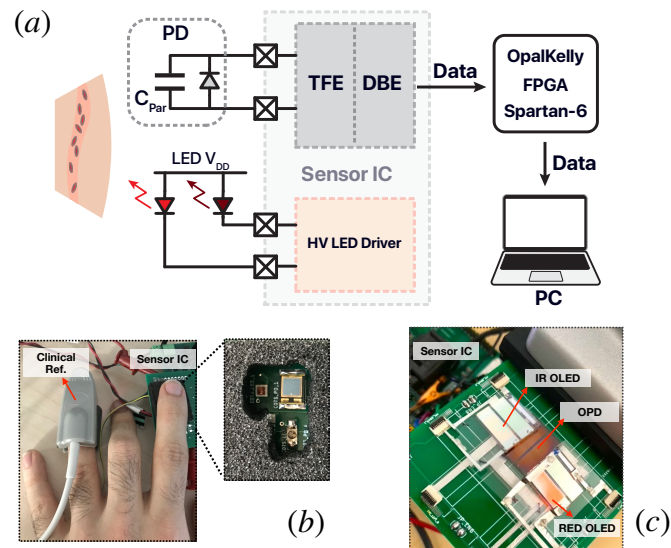
	Cont. Mode	Sparse Mode
LED V$_{DD}$ (V)	5	
Duty Cycle (%)	0.25	
LED Power (μW)	45.1	11.4
SpO$_2$ Error (%)	0.5	0.7
HR Error (bpm)	0.3	0.4

	Cont. Mode	Sparse Mode
OLED V$_{DD}$ (V)	8	
Duty Cycle (%)	0.5	
LED Power (μW)	727	182
SpO$_2$ Error (%)	0.35	0.5
HR Error (bpm)	0.3	0.4

Fig. 15. *In vivo* measurement setups (a) as well as a summary of the results when using (b) commercial silicon devices and (c) flexible organic devices.

This article has been accepted for publication in IEEE Transactions on Biomedical Circuits and Systems. This is the author's version which has not been fully edited and content may change prior to final publication. Citation information: DOI 10.1109/TBCAS.2022.3223971

IEEE TRANSACTIONS ON BIOMEDICAL CIRCUITS AND SYSTEMS 8

TABLE I
COMPARISON WITH PRIOR ARTS OF PPG AND SpO$_2$ SENSORS

Reference	ISSCC 2016 [8]	TBCAS 2017 [20]	TBCAS 2018 [21]	TBCAS 2019 [28]	TBCAS 2019 [15]	ISSCC 2021 [18]	TBCAS 2021 [27]	JSSC 2021 [19]	This work Continuous Mode	This work Sparse Mode
Technology (nm)	180	180	180	55	180	65	180	65	40 HV	
V$_{DD}$ (V) [LED/Readout]	5/1.5	5/1.2	3.3	2.8/1.2	3.3/1.8	1.8/1	3.3/1.2	-/0.6	5/1.1	
C_{Par} (pF)	1000	155	44	-	—^{g}	-	-	-	Si: 40 / OPD: 4800	
Readout Power (µW/Ch.)	87^a	172	27.4	54	9	24	28	0.532	TFE: 1.22 DBE: 3.34	TFE:0.32 DBE: 3.43
LED Power (µW/LED)	27^{a,d}	120^c	16	102.5	17.5	11.5	305	8.5	22.6	5.7
Total Power (µW/Ch.)	114	292	43.4	156.5	26.5	35.5^a	333	9.032	27.2	9.45
Sampling Freq. (Hz)	400	128	100	128	25	20	2048	20	100	
Duty Cycle (%)	2	0.4	0.25	-	0.7	0.04	1	1	0.25	
Input Noise (pA/$\sqrt{Hz}$)	-	153	-	6.3	-	-	8.7^a	20.1	4.8^e	
SpO$_2$ Error (%)	1.1^b	-	-	-	-	-	-	-	0.5^f	0.7^f
HR Error (bpm)	-	2^b	2^b	-	1.4^f	1.9^f	-	-	0.3^f	0.4^f

^{a}Estimated ^{b}Max. error ^{c} 10× Compression Rate ^{d}Organic LEDs/PDs ^{e} C_{par} = 40pF (Matching C_{pd}) ^{f}Mean Abs. error. ^{g} Low C_{Par} on-chip PD.

30 similar recordings of HR and SpO$_2$ measurements in sparse mode and compares the results against the clinical reference. The measured standard deviation of error for HR and SpO$_2$ recordings were 0.24 bpm and a 0.21% respectively.

A similar experiment was performed using a set of flexible organic devices discussed in [9], [10]. The OPD has a measured C_{Par} of 4.8 nF, less than 10 nA dark current at 0 V bias, and provides a quantum efficiency (QE) of ∼30-40% over the red and IR wavelengths [10]. The red and IR OLEDs exhibit about 5.7 nF and 6.2 nF of parasitic capacitance respectively and as shown in [10] require about 5-7 V of forward voltage at 10 mA of current. The PPG waveform, and the corresponding measured HR and SpO$_2$ are plotted in figure 14 in both continuous and sparse modes. The sensor achieved less than 1 bpm and less than 1% HR and SpO$_2$ errors when compared against the clinical reference. The use of organic devices required a higher drive voltage (8 V), an increased drive current as well as a higher (0.5%) duty cycle ratio resulting in overall higher power consumption. However, enabling sparse mode significantly lowered the OLED power by about 75%, improving sensor battery life. Figure 15 presents the measurement setup and a summary of the *in vivo* results using (a) commercial and (b) organic devices.

Figure 16 captures an incident where the sparse mode operation is interrupted by a motion artifact that is large enough to create a big difference in sampled PAV values compared to the previously captured PAVs. This causes an unwanted shift in the estimated period and results in the following PAVs to be missed. As shown in the figure, the sensor initially tries to find new PAVs by expanding the observation window and increasing W. Since no new PAVs are found after W reaches W$_{Max}$, the sensor eventually reverts to continuous mode. Shortly after this transition occurs, the backend re-learns the signal period and the system re-enters sparse mode.

VI. SUMMARY

A comparison against the most recent prior arts of PPG and SpO$_2$ sensors is provided in Table I. The LED power is normalized by the number of LEDs in the system since only a single wavelength PPG measurement is required to report HR, while SpO$_2$ requires two. The TFE power however is not normalized since there could be bias current variations between different phases of operation in prior arts. Compared to state-of-the-art, this work achieves the lowest LED power and one of the lowest total power consumptions while simultaneously delivering the lowest input referred noise. The measured HR and SpO$_2$ errors are less than 1 bpm and 1% respectively and are lower compared to other works.

The functionality and performance of the proposed sensor IC was characterized using both commercial and flexible organic interface devices. The *in vivo* measurement results confirm the accuracy of the sensor data when operating with a wide range of optical components including organic devices with parasitic capacitances as large as 10 nF. The introduction of reconstruction-free sparse sampling reduces the overall system power by nearly 70% while maintaining the accuracy of the output data.
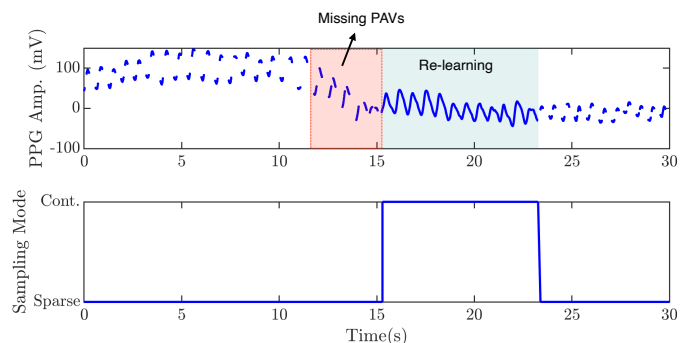

Fig. 16. Missing PAVs due to motion artifact creating a large change in the sampled PAV values. The backend initially expands W, then reverts to the continuous mode and finally re-gains lock on the PPG.

APPENDIX
NOISE ANALYSIS, ZTIA VS. CTIA

This section covers the analytical description of the TIA noise when operating with a large C_{Par} at the input. For simplicity, the core OTA is modeled as a single stage with a transconductance of g_m. Figure 17 shows the representative diagram of the discussed circuit. The two major sources of noise are the amplifier thermal noise modeled as a current source at the OTA output as well as the thermal noise of R_F. Each of these sources impact the TIA output voltage with their specific transfer functions, shown in simplified forms as follows (Eq. 6 & 7).

$$H_{v_{n_{R_F}}}(s) = \frac{C_{Par}s + g_m}{C_{Par}C_F R_F s^2 + (C_{Par} + C_F g_m R_F)s + g_m} \tag{6}$$

$$H_{i_{n_{gm}}}(s) = \frac{R_F(C_{Par} + C_F)s + 1}{C_{Par}C_F R_F s^2 + (C_{Par} + C_F g_m R_F)s + g_m} \tag{7}$$

The power spectral densities (PSD) of the two noise sources can be written as:

$$\frac{v_{n_{R_F}}^2}{\Delta f} = 4kTR_F, \qquad \frac{i_{n_{gm}}^2}{\Delta f} = 4kT\gamma\alpha g_m \tag{8}$$

Where α and γ are parameters relating to the technology and topology of choice and T is the absolute temperature. For simplicity, we assume $\alpha = 1$, $\gamma = 1$. This gives the following PSD for the TIA output noise:

$$S_{N_{out}}(f) \approx 4kT\left(\frac{1}{g_m} + R_F\right)$$

$$\times \left(\frac{4\pi^2 \frac{R_F}{g_m}C_{Par}^2 f^2 + 1}{16\pi^4 C_F^2 C_{Par}^2 \frac{R_F^2}{g_m^2}f^4 + 4\pi^2\left(\frac{C_{Par}^2}{g_m^2} + R_F^2 C_F^2\right)f^2 + 1}\right) \tag{9}$$

At low frequencies, the PSD has a value of,

$$S_{N_{out}}(f) \approx 4kT\left(\frac{1}{g_m} + R_F\right) \tag{10}$$

The shape of the PSD in (9) changes with the values of C_{Par} and C_F varying with respect to each other. As C_{Par} increases, the PSD begins to peak at higher frequencies. This high frequency noise can however be attenuated through the subsequent stages since it exceeds the observation bandwidth of the frontend. In this work, using a reset integrator as the following block (section IV-C), the required filtering can be achieved. The boxcar averaging applies a Sinc transfer function to the TIA output as follows [29].

$$H_{Sinc}(f) = \frac{T_{Int}}{R_{Int} \cdot C_{Int}} \cdot Sinc(T_{Int} \cdot f) \tag{11}$$

Integrating (9) when filtered by (11) will determine the variance of a single sample taken at the ADC output. (9) can also be used to find the noise PSD of the CTIA topology prior to sampling, via setting $R_F \to \infty$, resulting in:

$$S_{N_{out_{CTIA}}}(f) = 4kT\frac{1}{g_m} \cdot 1/\left(4\pi^2\frac{C_F^2}{g_m^2}f^2 + \frac{C_F^2}{C_{Par}^2}\right) \tag{12}$$
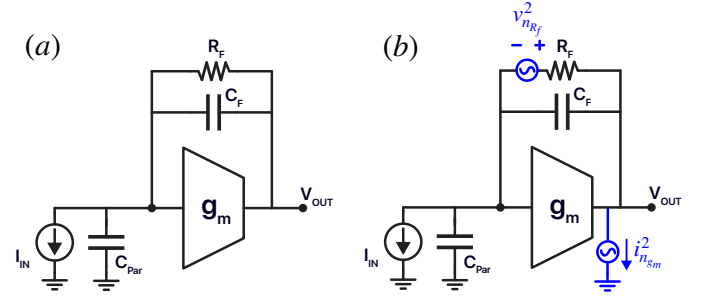

Fig. 17. Simplified diagram of the ZTIA used for the analysis (a). The noise sources of the OTA and RF are shown in (b).
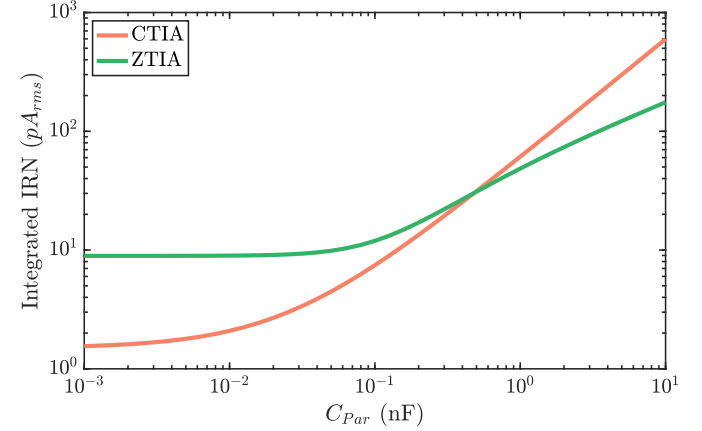

Fig. 18. The input referred standard deviation of a single sample taken in ZTIA and CTIA schemes versus C_{Par}.

At low frequencies, the OTA input referred voltage noise is boosted by a factor of C_{Par}/C_F at the CTIA output, highlighting the issue of CTIA topology in handling large C_{Par}. In practice, CTIA designs require reset phases inducing reset kT/C noise which will then be removed via CDS. [17] provides a comprehensive analysis of this scheme. The effective output noise PSD of that scheme can be found as:

$$S_{N_{CDS}}(f) = 2(\pi f_C T_{Int} - 1)\left(1 + \frac{C_{Par}}{C_F}\right)^2$$
$$\times 4kT\frac{1}{g_m} \cdot Sinc^2(T_{Int} \cdot f) \tag{13}$$

where f_C is the closed loop bandwidth of the CTIA. By integrating this PSD, one can find the variance of a sample at the CTIA output. Figure 18 shows the variance of samples taken in both CTIA and ZTIA schemes when C_{Par} changes from 1 pF to 10 nF. The following parameter values were used to produce the graph: $g_m = 2$ mS, $TI_{gain} = 2$ $M\Omega$, and $T_{Int} = 50$ μs, which are typical numbers in the application. For both schemes, similar effective gain, T_{Int}, and g_m are assumed to deliver a fair comparison. This ensures that the same input can be amplified through the chain over the same observation window and using the same TIA power. Thus, based on the comparison results and since this work aims to acquire current out of a wide range of PDs with potentially very large C_{Par}, the ZTIA scheme is selected in the design.

REFERENCES

[1] Aliverti, Andrea. "Wearable technology: role in respiratory health and disease." Breathe 13.2 (2017): e27-e36.

[2] Alvarez, Paulino, et al. "Chronic disease management in heart failure: focus on telemedicine and remote monitoring." Reviews in Cardiovascular Medicine 22.2 (2021): 403-413.

[3] Un, Ka-Chun, et al. "Observational study on wearable biosensors and machine learning-based remote monitoring of COVID-19 patients." Scientific reports 11.1 (2021): 1-9.

[4] Mck, Julia E., et al. "Market and patent analyses of wearables in medicine." Trends in biotechnology 37.6 (2019): 563-566.

[5] Dunn, Jessilyn, Ryan Runge, and Michael Snyder. "Wearables and the medical revolution." Personalized medicine 15.5 (2018): 429-448.

[6] Tersalvi, Gregorio, et al. "Telemedicine in heart failure during COVID-19: a step into the future." Frontiers in Cardiovascular Medicine 7 (2020): 612818.

[7] Lochner, Claire M., et al. "All-organic optoelectronic sensor for pulse oximetry." Nature communications 5.1 (2014): 1-7.

[8] Lee, Yongsu, et al. "22.3 A 141W sensor SoC on OLED/OPD substrate for SpO$_2$/ExG monitoring sticker." 2016 IEEE International Solid-State Circuits Conference (ISSCC). IEEE, 2016.

[9] Khan, Yasser, et al. "A flexible organic reflectance oximeter array." Proceedings of the National Academy of Sciences 115.47 (2018): E11015-E11024.

[10] Jan, Jasmine, et al. "Flexible BladeCoated Optoelectronic Devices: Dual Functionality via Simultaneous Deposition." Advanced Functional Materials (2022): 2112343.

[11] Chen, Shuwen, et al. "Flexible wearable sensors for cardiovascular health monitoring." Advanced Healthcare Materials 10.17 (2021): 2100116.

[12] Yin, Da, et al. "Highly transparent and flexible fabric-based organic light emitting devices for unnoticeable wearable displays." Organic Electronics 76 (2020): 105494.

[13] Jansenvan Vuuren, Ross D., et al. "Organic photodiodes: the future of full color detection and image sensing." Advanced Materials 28.24 (2016): 4766-4802.

[14] Someya, Takao, et al. "Integration of organic FETs with organic photodiodes for a large area, flexible, and lightweight sheet image scanners." IEEE transactions on electron devices 52.11 (2005): 2502-2511.

[15] Caizzone, Antonino, Assim Boukhayma, and Christian Enz. "A 2.6μ W Monolithic CMOS Photoplethysmographic (PPG) Sensor Operating With 2μ W LED Power for Continuous Health Monitoring." IEEE Transactions on Biomedical Circuits and Systems 13.6 (2019): 1243-1253.

[16] Sharma, Ajit, et al. "A Sub-60-μA Multimodal Smart Biosensing SoC With > 80-dB SNR, 35-μA Photoplethysmography Signal Chain." IEEE Journal of Solid-State Circuits 52.4 (2017): 1021-1033.

[17] Crescentini, Marco, et al. "Noise limits of CMOS current interfaces for biosensors: A review." IEEE transactions on biomedical circuits and systems 8.2 (2013): 278-292.

[18] Jung, Sung-jin, et al. "28.2 A 400-to-1000nm 24μ W monolithic PPG sensor with 0.3 A/W spectral responsivity for miniature wearables." 2021 IEEE International Solid-State Circuits Conference (ISSCC). Vol. 64. IEEE, 2021.

[19] Agarwala, Rishika, et al. "A 0.6 V 785-nW multimodal sensor interface IC for ozone pollutant sensing and correlated cardiovascular disease monitoring." IEEE Journal of Solid-State Circuits 56.4 (2021): 1058-1070.

[20] Pamula, Venkata Rajesh, et al. "A 172μ W Compressively Sampled Photoplethysmographic (PPG) Readout ASIC With Heart Rate Estimation Directly From Compressively Sampled Data." IEEE transactions on biomedical circuits and systems 11.3 (2017): 487-496.

[21] Lee, Jinseok, et al. "A low-power photoplethysmogram-based heart rate sensor using heartbeat locked loop." IEEE transactions on biomedical circuits and systems 12.6 (2018): 1220-1229.

[22] Faraji Alamouti, Sina , et al. "An SpO$_2$ Sensor Using Reconstruction-Free Sparse Sampling for 70% System Power Reduction." 2022 IEEE International Solid-State Circuits Conference (ISSCC). Vol. 65. IEEE, 2022.

[23] Moo, Andreia V., Sander Stuijk, and Gerard de Haan. "New insights into the origin of remote PPG signals in visible light and infrared." Scientific reports 8.1 (2018): 1-15.

[24] Schnle, Philipp C. A power efficient spectrophotometry & PPG integrated circuit for mobile medical instruments. Diss. ETH Zurich, 2017.

[25] Glaros, Konstantinos N., and Emmanuel M. Drakakis. "A sub-mW fully-integrated pulse oximeter front-end." IEEE transactions on biomedical circuits and systems 7.3 (2012): 363-375.

[26] Wukitsch, Michael W., et al. "Pulse oximetry: analysis of theory, technology, and practice." Journal of clinical monitoring 4.4 (1988): 290-301.

[27] Lin, Qiuyang, et al. "A 134 dB dynamic range noise shaping slope Light-to-Digital converter for wearable chest PPG applications." IEEE Transactions on Biomedical Circuits and Systems 15.6 (2021): 1224-1235.

[28] Song, Shuang, et al. "A 769 μW battery-powered single-chip SoC with BLE for multi-modal vital sign monitoring health patches." IEEE Transactions on Biomedical Circuits and Systems 13.6 (2019): 1506-1517.

[29] Ezekwe, Chinwuba D., and Bernhard E. Boser. "A Mode-Matching $\Sigma\Delta$ Closed-Loop Vibratory Gyroscope Readout Interface With a $0.004°/s/\sqrt{Hz}$ Noise Floor Over a 50 Hz Band." IEEE Journal of Solid-State Circuits 43.12 (2008): 3039-3048.

Sina Faraji Alamouti received the B.S. degree in electrical engineering from the Sharif University of Technology, Tehran, Iran, in 2016, and the M.S. degree in electrical engineering from the University of California at Berkeley, Berkeley, CA, USA, in 2020, where he is currently pursuing the Ph.D. degree in electrical engineering and computer sciences. His research interests include design of analog/mixed-signal integrated circuits and systems and for biomedical applications. Mr. Faraji Alamouti was a recipient of the UC Berkeley EECS Department Fellowship in 2016 and the ADI Outstanding Student Designer Award in 2019.

Jasmine Jan is a PhD student in the Electrical Engineering and Computer Sciences Department at the University of California, Berkeley. She is currently researching printed organic optoelectronics. She received a Master of Science in Electrical Engineering and Computer Sciences in 2020 and Bachelor of Science in Bioengineering at the University of California, Berkeley.

Cem Yalcin received the B.Sc. and M.S. degrees in Electrical and Electronics Engineering from Middle East Technical University, Ankara, Turkey, in 2013 and 2016 respectively. From 2013 to 2017, he worked as an IC Design Engineer in Mikro-Tasarim. He is currently a PhD candidate in Electrical Engineering and Computer Sciences at University of California at Berkeley, Berkeley, CA, USA. His current research interests include actuation and array-scale driving of MEMS mirrors, spatial light modulators and computer-generated holography.

Jonathan Ting received the B.S. degree in electrical engineering from the Georgia Institute of Technology, in 2015 and the Ph.D. degree from the Department of Electrical Engineering and Computer Sciences, University of California, Berkeley, from Professor Ana Claudia Arias research group in 2021. His research interests primarily include flexible wearable sensors, with a focus in printed opto-electronics and biosensors.

Ana Claudia Arias received her PhD in Physics from the University of Cambridge, UK in 2001. Prior to that, she received her master and bachelor degrees in Physics from the Federal University of Paran in Curitiba, Brazil in 1997 and 1995 respectively. She joined the University of California, Berkeley in January of 2011. Prof. Arias was the Manager of the Printed Electronic Devices Area and a Member of Research Staff at PARC, a Xerox Company. She went to PARC, in 2003, from Plastic Logic in Cambridge, UK where she led the semiconductor group. Her research focuses on the use of electronic materials processed from solution in flexible electronic systems. She uses printing techniques to fabricate flexible large area electronic devices and sensors.

Rikky Muller , PhD is an Associate Professor of Electrical Engineering and Computer Sciences at UC Berkeley where she holds the S. Shankar Sastry Professorship in Emerging Technologies. She received her BS and Meng degrees from MIT and her PhD from UC Berkeley. She is currently a Co-director of the Berkeley Wireless Research Center (BWRC), a Core Member of the Center for Neural Engineering and Prostheses (CNEP) and an Investigator at the Chan-Zuckerberg Biohub. Dr. Muller was previously an IC designer at Analog Devices, and was the co-founder of Cortera Neurotechnologies, Inc. (acq. 2019) a medical device company focused on closed-loop deep brain stimulation technology. Her research group focuses on emerging implantable and wearable medical devices and in developing low-power, wireless microelectronic and integrated systems for neurological applications. Dr. Muller received her BS and MS degrees from MIT and her Ph.D. from UC Berkeley all in EECS. She was a McKenzie Fellow and Lecturer of EE at the University of Melbourne in Australia. She was named one of MIT Tech Reviews 35 global innovators under 35 (TR35) and Boston MedTechs 40 healthcare innovators under 40. She is the recipient of the National Academy of Engineering Gilbreth Lectureship, the NSF CAREER Award, the Keysight Early Career Professorship, the McKnight Technological Innovations in Neuroscience Award, and the IEEE Solid-State Circuits Society New Frontier Award. She is a Bakar Fellow, a Hellman Fellow, and served as Distinguished Lecturer for the Solid-State Circuits Society. Dr. Muller is the IMMD Subcommittee Chair for IEEE ISSCC and has previously served on the technical program committees of IEEE CICC and BioCAS. She is a member of the SSCS Advisory Committee, the Solid State Circuits Directions Committee, and Women in Circuits. She is the co-organizer of the IEEE Brain Discovery Neurotechnology Workshop. She has also served as a guest editor for the IEEE Journal of Solid-State Circuits.